ICAS-90-1.5.2

OPTIMAL REENTRY TRAJECTORIES YIELDING REDUCED ABSORBED HEAT AND EXTENDED CROSS RANGE

M.K. Horn
Messerschmitt-Bölkow-Blohm
8012 Ottobrunn, FRG

Abstract

Optimal reentry trajectories yielding both low absorbed heat and large cross range are presented. These trajectories consist of the deorbit phase and the atmospheric flight down to an altitude of 24.5 km. Temperature constraints as well as hinge moment, dynamic pressure, and load factor limits are considered throughout the entire flight path, and specified end conditions (Mach number = 2, altitude = 24.5 km) are satisfied. The structure of the optimal trajectories is compared to that of similar trajectories based on an engineering approach for selecting the control functions, showing a reduction of more than 20% in the absorbed heat per cross range. This reduction is achieved (1) by the selection of an optimal flight path angle at atmospheric interface combined with a variable angle of attack profile in the early stages of atmospheric flight and (2) by the inclusion of a sequence of flare-dive segments during the remainder of the trajectory. No-skip trajectories are first analyzed, and then slight skipping is permitted to indicate potential in reducing the total absorbed heat when slight altitude increases are allowed. The optimization package for determining the trajectories is discussed, particulary features which are critical in analyzing such flight paths.

I. Introduction

Optimal reentry trajectories are investigated from the deorbit point to the onset of the terminal area energy management phase (TAEM). These trajectories link the deorbit phase to the atmospheric flight down to 24.5 km, selecting the control functions and design parameters such that the trajectories yield low absorbed heat and large cross range. Constraints imposed throughout the entire flight path are that: (1) temperature, (2) dynamic pressure, (3) hinge moment, and (4) load factor limits may not be violated. These bounds can be expressed as a function of altitude, velocity, and angle of attack, α. Conditions to be met at the end of the trajectory are: Mach number = 2 and altitude = 24.5 km. Non-skip trajectories are first considered, and then slight skipping is permitted to indicate the potential of such a strategy in reducing the total absorbed heat.

The motivation behind the current research is: to analyze reentry trajectories by means of an "objective" optimization software package to determine what parameters and what control function strategies can be effective in reducing absorbed heat and in extending cross range. These results are to serve as input for modifications to an existing trajectory analysis developed using an engineering approach for selecting the control functions and design parameters.(1)(2) The optimal trajectories determined in this report are compared to the "nominal trajectories" of Reference 1. The optimal flight paths show an improvement of more than 20% compared to these nominal trajectories when considering the cost function: total absorbed heat per cross range. Thus, for example, for essentially the same cross range, a substantial reduction in absorbed heat can be achieved.

The optimal flight paths differ in structure from the nominal trajectories, employing a variable α control in the early portion of the atmospheric flight to affect a higher initial flare. After this flare, the remainder of the trajectory consists of a sequence of flare-dive segments which yield better braking/cooling effects than does the smooth descent technique of the nominal flight path. The third critical difference in the two strategies involves the selection of the burn time (braking effect) in the deorbit phase which is used to establish conditions at the atmospheric interface (120 km). The resulting γ-entry value (along with the corresponding state conditions) is shown to be an effective parameter in reducing the total absorbed heat.

A parameterized optimization package(2)(3) has been used to generate the optimal trajectories. The angle of attack, α, and roll angle, μ, are defined as continuous functions of time, using the discrete points from the optimization code. Additional optimization parameters are used to define (scalar) design parameters: (1) the total time for the atmospheric flight and (2) the burn time for the deorbit phase. Still another set of the points is used to define critical time points in the control functions (moveable grid points), namely: (1) the onset of sudden changes in the control functions, (2) the positioning of maximum/minimum control values, and (3) the relaxation of constraints imposed on the controls. The optimization package is discussed, particularly the features which are critical in analyzing such trajectories.

The mathematical model is presented in Section II. A general discription of the structure of the optimal trajectories is found in Section III, with the optimization code and its features relating to the structure of the flight paths being described in Section IV. Numerical results are presented in Section V; the conclusions, in Section VI.

II. Mathematical Model

The reentry trajectories are determined using a point mass model with complete aerodynamic characteristics but with no moments of inertia. The equations of motion include earth rotation and oblateness effects as well as both radial and lateral components of the gravitational force. The heat flux model is based on the Detra/Kemp/Riddel cold wall model (with reference radius 1 meter). The 1966 U.S. Standard atmosphere has been used.

The equations of motion are:

$$\begin{aligned} dV/dt = \; & R * \Omega^2 * (\cos\delta * \cos\delta * \sin\gamma \\ & - \sin\delta * \cos\delta * \cos\gamma * \cos\chi) \\ & - g_{radial} * \sin\gamma - g_{lateral} * \cos\chi * \cos\gamma \\ & + (T * \cos(\alpha + \varepsilon) - D)/m \end{aligned} \tag{1}$$

$$\begin{aligned} d\chi/dt = \; & V * \cos\gamma * \sin\chi * \tan\delta / R \\ & + 2 * \Omega * (\sin\delta - \cos\chi * \cos\delta * \tan\gamma) \\ & + (R * \Omega^2 * \sin\chi * \sin\delta * \cos\delta / \cos\gamma \\ & + g_{lateral} * \sin\chi) / V + (T * \sin(\alpha+\varepsilon) \\ & + L) * \sin\mu / (V * m * \cos\gamma) \end{aligned} \tag{2}$$

$$\begin{aligned} d\gamma/dt = \; & (V * \cos\gamma) / R + 2 * \Omega * \sin\chi * \cos\delta \\ & + (R * \Omega^2 * (\cos\delta * \cos\delta * \cos\gamma \\ & + \sin\delta * \cos\delta * \sin\gamma * \cos\chi) \\ & - g_{radial} * \cos\gamma + g_{lateral} * \cos\chi * \sin\gamma \\ & + (T * \sin(\alpha+\varepsilon) + L) * \cos\mu)/m) / V \end{aligned} \tag{3}$$

$$d\tau/dt = V * \cos\gamma * \sin\chi / (R * \cos\delta) \tag{4}$$

$$d\delta/dt = V * \cos\gamma * \cos\chi / R \tag{5}$$

$$dR/dt = V * \sin\gamma \tag{6}$$

$$dQ/dt = \text{const} * \sqrt{\rho} * V^3 \tag{7}$$

where the state variables are: V = speed, χ = heading angle, γ = flight path angle, τ = longitude, δ = latitude, R = radius, and Q = absorbed heat (at the stagnation point). $\dot{Q} = dQ/dt$ is referred to as the heat flux. Altitude, $h = R - Re(\delta)$, i.e., the difference between R and the radius of the earth given as a function of δ. The thrust vectoring angle, ε, is zero.

The remaining parameters are: Ω = the earth's rotation, g_{radial} and $g_{lateral}$, the radial and lateral components of gravity, respectively, T = thrust, D = drag, L = lift, const = .00000017 (giving heat flux in KW/m^2). Control functions, α and μ, (angle of attack and roll angle), are to be selected as functions of time by the optimization package. (Units: MKS system)

III. General Characteristics of the Optimal Reentry Trajectory

The reentry trajectories considered have two principal phases: (1) the deorbit phase, from the deorbit point to the atmospheric interface (120 km), and (2) the atmospheric phase, from 120 km down to the onset of the TAEM, i.e., 24.5 km. Aerodynamic effects are included throughout the entire trajectory but play no significant role in the deorbit phase (and actually have little effect during the first 15 km of the atmospheric segment). Thrust, used to brake the spacecraft, is available only at the start of the deorbit phase, with the length of the burn time to be determined by the optimization package. Both angle of attack, α, and roll angle, μ, are available as controls to be determined by the optimization package as functions of time. In addition, both (1) the total flight time for the atmospheric flight and (2) the burn time enter the optimization problem as (scalar) design parameters to be determined.

This section gives a general description of the characteristics of the optimal reentry trajectories. Numerical details are discussed in Section V.

Deorbit Phase

The reference orbit considered is a circular orbit (radius = 450 km) with inclination 28.5°. Longitude and latitude at the deorbit point are: τ = -140.0° and δ = -28.5°, respectively. The mass at the deorbit point is 29,000 kg. After braking, the tank along with the remainder of the fuel is cast off, and the mass of the vehicle becomes 26,000 kg. Thrust during braking is directed opposite to the flight direction. After braking, the vehicle is assumed to be turned instantaneously (180°) for the reentry flight. Angle of attack after the burn has been set at 25 deg simply for comparison with the nominal trajectories. (The value of α plays no significant role during the deorbit phase because aerodynamic effects are negligible.) Roll angle, μ, is zero during this phase.

Optimization Parameters during the Deorbit Phase. Only one parameter is effective during the deorbit phase, namely the burn time. The length of the burn results in a particular state condition at an altitude of 120 km, i.e., in specific V, χ, γ, τ, δ, and R values at the atmospheric interface. From a practical stand point, however, one speaks of γ-entry, i.e., γ at 120 km, as the optimization parameter, since physically the term is more relevant than the burn time. More specifically, γ-entry defines the angle at which the spacecraft dives into the atmosphere and thus has a dominant effect on the heat build-up. In addition, the value γ-entry is to be limited: $-1.4° \le \gamma\text{-entry} \le -1.2°$. When γ-entry is given as the optimization parameter, then the corresponding state (i.e., V, χ, τ, δ, and R) is also used, all of which are related to a specific burn time.

Deorbit Phase Formulation for the Optimization Process. If the deorbit is to be initiated from a specified deorbit point, the results of the deorbit phase can be expressed in tabular form with V, χ, τ, δ, and R as functions of γ at the atmospheric interface (all denoted with subscript "entry"), and γ-entry can be used as the optimization parameter. These results can be processed *a priori* and used for different applications during the atmospheric portion of the flight, thus, saving considerable computing time and yet still giving optimal trajectories over the entire flight path from the deorbit point to the TAEM onset. (See Table 1.)

If the deorbit point is to be located optimally, e.g., in order to reach a specified landing site, then similar tables can be generated for a sequence of deorbit points. This approach can also be performed *a priori* resulting in the same state variables being expressed as functions of two variables, say, τ-deorbit and γ-entry, both of which enter the optimization process as design parameters to be selected optimally.

Conditions at Atmospheric Interface (120 km)					
γ	V	χ	τ	δ	R
-1.40	7.5003	66.38	18.23	-21.13	6496.06
-1.38	7.5008	66.59	18.48	-20.54	6496.00
-1.36	7.5014	66.80	18.72	-19.96	6495.94
-1.34	7.5019	66.02	18.96	-19.36	6495.89
-1.32	7.5024	66.24	19.19	-18.76	6495.83
-1.30	7.5029	66.46	19.43	-18.16	6495.77
-1.28	7.5034	66.70	19.67	-17.55	6495.72
-1.26	7.5040	66.94	19.90	-16.94	6495.67
-1.24	7.5044	66.18	20.14	-16.32	6495.61
-1.22	7.5049	66.42	20.37	-15.70	6495.55
-1.20	7.5054	66.67	20.60	-15.07	6495.50

Table 1. Deorbit Phase Results: State Variables at Atmospheric Interface Resulting from Different Burn Times.

Deorbit Phase Design Parameter for the Nominal Trajectories. In determining the nominal trajectories, the burn time is selected using a different criteria from that of the optimal flight paths, but still with the intent to control the total absorbed heat. For the nominal flight paths, the burn time is chosen to produce a γ-entry which results in a specified *maximum* heat flux. Since the nominal flight path strategy maintains a long flight span along the $\dot{Q}$ max bound, such a burn time selection is appropriate for the strategy assumed. However, using γ-entry to control the total absorbed heat directly can be shown to be more effective.

Atmospheric Flight down to TAEM

During the atmospheric flight both angle of attack, α, and roll angle, μ, are available as control functions in time. In addition, the total time of the atmospheric flight is used as an optimization parameter The initial conditions for this phase are variable, expressed as functions of γ-entry (or γ-entry and τ-deorbit) resulting from the length of the burn time (and from the deorbit point), generated during the deorbit phase.

Altitude-Velocity diagrams (Figs. 1 and 3) show the basic structure of the trajectories while the area under the the heat flux vs time curves (Figs. 2 and 4) gives the total absorbed heat during the flight.

The Initial Flare in Atmospheric Flight. The control functions are not effective above 100 km and are still only marginally effective above 90 km. The spacecraft dives until it reaches an altitude of somewhat less than 90 km at which point the aerodynamic forces are large enough to enable the vehicle to flare. During roughly the first 200 sec of the atmospheric flight the value of γ-entry plays the dominant role in controlling heat flux; afterwards the value of the control functions, i.e., the placement of the initial flare, contributes significantly to the heat flux control.

The Flare-Dive Strategy of the Optimal Trajectories. The remainder of the flight consists of a sequence of flare-dive segments which is an effective braking/

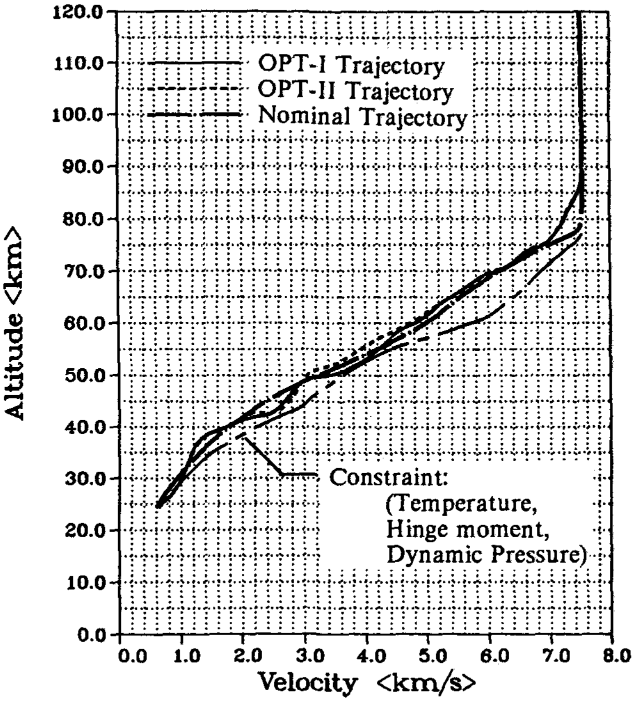

Fig. 1. Altitude-Velocity profiles for the OPT-I, OPT-II, and nominal trajectories.

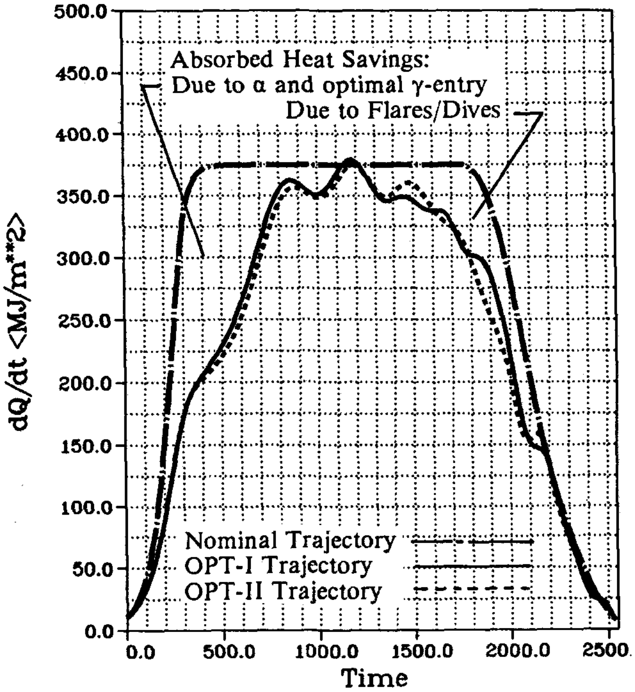

Fig. 2. Heat flux as a function of time for the OPT-I, OPT-II, and nominal trajectories. (Total absorbed heat = area under the curves.)

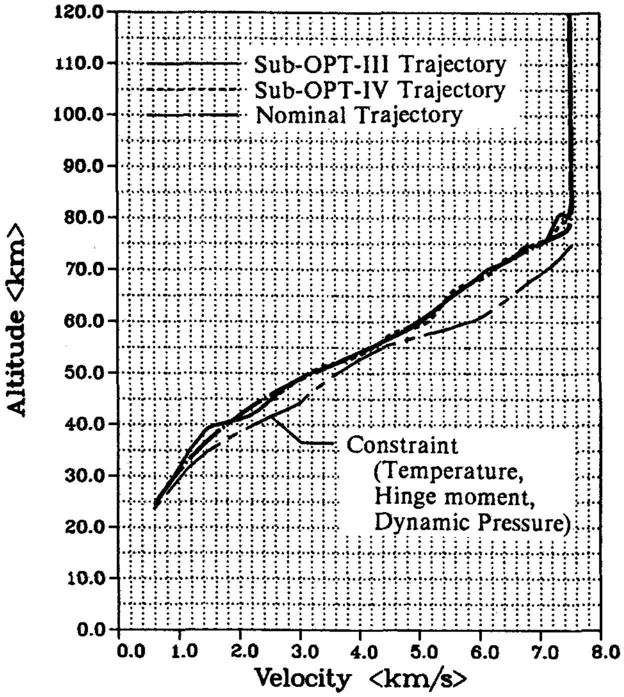

Fig. 3. Altitude-Velocity profiles for the Sub-OPT-III, Sub-OPT-IV, and nominal trajectories.

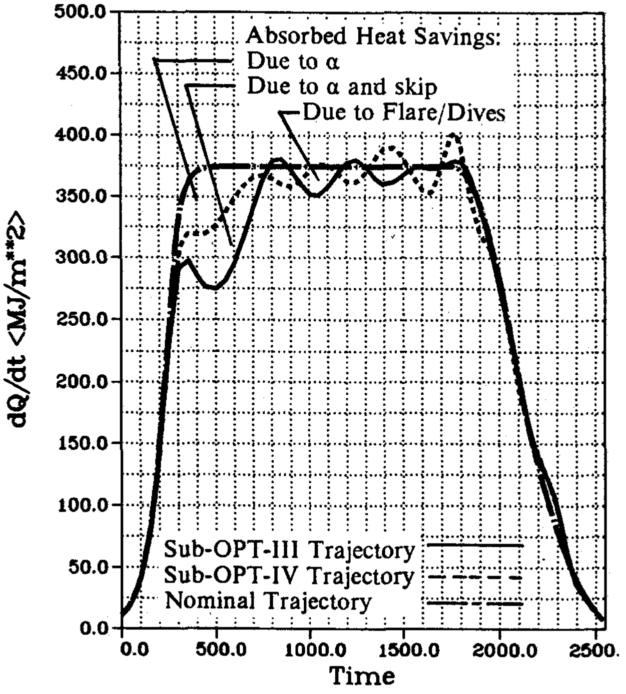

Fig. 4. Heat flux as a function of time for the Sub-OPT-III, Sub-OPT-IV, and nominal trajectories. (Total absorbed heat = area under the curves.)

cooling technique. Since the heat flux (Eqn. 7) is proportional to V^3, reducing the velocity as soon as possible is a primary goal during the optimization process. (See Fig. 8 .) The air density is the second critical parameter in controlling the heat flux. Thus, the optimal combination of altitude and velocity controls the total absorbed heat, i.e., the area under the heat flux curve. The dive segments affect the braking; the flare segments control the cooling.

The flare-dive structure of the optimal solution and the smoother descent of the nominal solution is clearly evident in the altitude-velocity diagrams.

Constraints during Atmospheric Flight. Constraints, formulated as an altitude limit expressed in terms of V and α, are imposed during the atmospheric flight. (See Figs. 1 and 3.) At high velocities, temperature constraints limit the minimum allowable altitude. As the velocity decreases, hinge moment constraints come into effect, and eventually dynamic pressure limits. A load factor constraint is also considered but the contribution to the constraint envelope lies within the dynamic pressure bounds.

An additional constraint may need to be imposed on the angle of attack, namely a thermal-α corridor. The minimum value of α is bounded by 25° when the heat flux is at high values. This bound is first relaxed when $\dot{Q}$ is below a specified value. For the current investigation, an arbitrary value of $\dot{Q} = 175$ KW/m^2 has been selected. Optimal trajectories have been determined with and without this thermal-α corridor. Imposing this α restriction produces optimal trajectories with less absorbed heat, but the cross range also suffers. The cost function, minimum total absorbed heat per cross range, suffers about a 2% increase if the thermal-α corridor is imposed.

IV. The Optimization Program -- STOMP

The optimal trajectories have been developed by applying a system of software packages:

1. SLLSQP - Sequential Linear Least Squares Programming,† a parameterized optimization package,
2. STOMP - (Speedy) Trajectory Optimization by Mathematical Programming,(2) a modified version of the TOMP‡ program,(3) and
3. RKF45T - a fifth order Runge-Kutta-Fehlberg integration package.(4) (5)

The STOMP Program

STOMP serves as the interfacing subroutine between the user and the parameterized optimization

---

† SLLSQP is an unpublished program due to D. Kraft, DLR-Oberpfaffenhofen, FRG, and K. Schittkowski, University of Bayreuth, Bayreuth, FRG.

‡ SLLSQP and TOMP packages, as well as the extensions to the RKFST package to include the root-solver have been developed and supplied by the Institut for Flight Systems Dynamics, DLR Oberpfaffenhofen, 8031 Wessling/Obb, FRG. The STOMP program has been extended and developed at MBB.

package. More specifically, the physically irrelevent "points" of the SLLSQP package are transformed into continuous control functions (e.g., α and μ) along with scalar design parameters (e.g., burn time) and are given to the user for evaluating the physical system. Derivatives required by the SLLSQP program are generated internally (numerically) within the the STOMP package, and the user simply solves the equations of motion repeatedly, using the updated control functions and design parameters supplied by the STOMP package.

The Control Function Definition in Program STOMP. The STOMP program defines continuous control functions in terms of the discrete points from the SLLSQP package. The user specifies a time grid (referred to as grid points), i.e., distinct points on a normalized time scale. Parameters from the SLLSQP package are then used to define the control function at these grid points. (See Fig. 5.) In addition, (1) any number of grid points may themselves be designated as "movable", i.e., they too enter the SLLSQP parameter set, and (2) any number of control function points may be designated as "fixed" (and do not enter the SLLSQP parameter set). All movable points are adjusted by the SLLSQP package to produce the optimal trajectories. All fixed points enter the control function definition but remain unchanged during the optimization process.

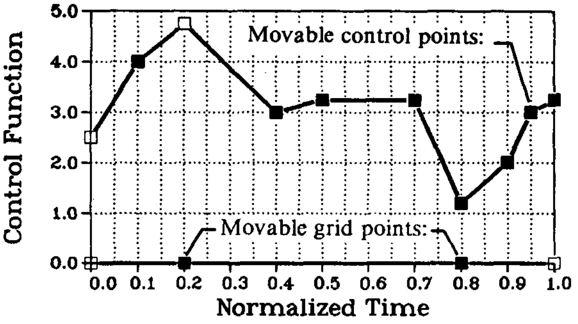

Fig. 5 STOMP control function structure: Example of a control function with both fixed and movable control points and grid points.

The STOMP program formulates the network of discrete points which are used to define the controls and then constructs continuous functions in time by using:

1. linear segments (with slope discontinuities at the grid points), e.g., $\mu(t)$ in Fig. 7,
2. spline functions (with continuous first and second derivatives at the grid points), or
3. spline-line functions (with a user-defined combination of linear and spline sub-segments), e.g., $\alpha(t)$ in Fig. 6.

The user supplies the initial guess for each of the grid points and control points (whether fixed or movable). During the optimization process STOMP updates all movable points and forms the control functions, supplying the user with the actual control value at the specific time. The user is not burdened with the control function definition but does have access to the entire function (and derivatives) in case this information is needed.

Special STOMP Control Function Features -- movable grid points. The movable grid points serve as a particularly useful tool in determining optimal trajectories. Four important applications critical in determining reentry trajectories are:

1. the positioning of sudden control function changes, e.g., the optimal location of the sudden onset of the roll angle, μ, during the initial dive into the atmosphere (γ build-up control), Fig. 7,
2. the positioning of local maxima or minima of the control function values, e.g., the positioning of the minimum value of μ and maximum value of α, to enact the initial flare (heat flux control and temperature constraint bound), Figs. 6 and 7,
3. the positioning of release points for control constraints, e.g., the positioning of the release point for the thermal-α corridor, and
4. the positioning of a sequence of near discontinuities in a control function, e.g., a sequence of roll reversals to fly an essentially straight ground track for reaching a specific landing site.

   Note: such roll reversals can also be useful in large cross range trajectories by imposing them at the end of the trajectory to increase the cross range by flying "directly away" from the orbit ground track. This technique, however, is not useful in the current application because nearly the entire time span is required to brake the spacecraft and to reduce the altitude. Little time is left over at the end to increase the cross range through roll reversals.

The movable grid point feature (1) improves the accuracy in modeling the optimal solution and at the same time (2) reduces computing time in determining the trajectories.

The RKF45T Program

The integration package for solving the equations of motion uses a 5th order Runge-Kutta-Fehlberg method, which has an embedded 4th order solution for step size control. The program has an efficient root-solver included which enables the user to isolate the time points associated with a state (or a state and derivative) related condition. Two examples of such root-solving applications in determining optimal trajectories are:

1. Isolating Skipping Points: A trajectory is said to "skip" when $\gamma > 0$. If the user wants to locate the points at which $\gamma = 0$, the expression can be given as a stopping condition for the integrator, and the precise time span of the skipping violation can be identified. In addition, $d\gamma/dt = 0$ identifies the time points for evaluating the local maximum and minimum altitude values and can be used to measure the magnitude of the skip.

   A violation can then be defined in terms of the time duration and/or the magnitude of the skip. This violation is imposed as a boundary condition to be driven to zero by the optimization package. By such a technique one can define no-skip or limited-skipping trajectories.

2. Isolating the Release Point for a Control Constraint: The thermal-α corridor is in effect until the heat flux reaches a specified level, i.e., until $\dot{Q} = 175$ KW/m^2. A movable grid point, t*, can be designated as the last point at which the control function is bounded by the constraint. The optimizer must then place this grid point at the state-related condition, $\dot{Q} = 175$ KW/m^2. The RKF45T package identifies the time point, t_{cr}, at which $\dot{Q}$ reaches the critical value. The expression, $(t_{cr} - t^*) > 0$, is given as a boundary condition to be satisfied by the SLLSQP package. If $t_{cr} > t^*$, the thermal-α corridor has not been violated. If $t_{cr} < t^*$, a penalty is imposed which the optimization package drives to zero by driving t_{cr} to the t* value.

V. Numerical Results

Optimal trajectories are presented for two types of flight paths: (1) with a thermal-α corridor imposed (i.e., with the constraint $\alpha > 25°$ for $\dot{Q} > 175$ KW/m^2), and (2) with no thermal-α corridor restriction. These results are compared with the nominal trajectories from Reference 1. Three basic differences exist between the optimal and nominal flight paths:

1. the selection of γ-entry,
2. the altitude of the initial flare (and the α-profile for generating the flare), and
3. the flare-dive sequence of the optimal trajectory (in contrast to the smoother descent of the nominal flight path).

The first two differences in strategy result in lower heat flux values through density effects (i.e.,the optimal trajectory flies at a higher altitude), while the flare-dive strategy results in improved braking/cooling.

Two additional sub-optimal paths are presented in which γ-entry is set at the nominal trajectory value (-1.4°) rather than being selected by the optimization process. These flight paths have substantially higher absorbed heat which is clearly evident by comparing Figs. 2 and 4. A slight skip is permitted during the hypersonic flare in one of the sub-optimal trajectories resulting in a reduction in total absorbed heat.

The four trajectories presented are designated:

OPT-I:	optimal solution with no thermal-α corridor
OPT-II:	optimal solution a thermal-α corridor imposed
Sub-OPT-III:	suboptimal no-skip solution (non-optimal γ-entry), and
Sub-OPT-IV:	suboptimal slight-skip solution (non-optimal γ-entry).

Numerical results showing the total absorbed heat, the cross range, and the value of the actual cost function, "absorbed heat per cross range", are presented for all four flight paths and for the nominal trajectory. Emphasis is placed on the OPT-I solution, with a discussion of the effects of imposing the thermal-α corridor. Sub-OPT-III and -IV are included to illustrate the importance of the proper selection of γ-entry.

Altitude-Velocity profiles are presented in Fig. 1 for the OPT-I, -II, and nominal trajectories and in Fig. 3 for the Sub-OPT-III, -IV, and nominal flight paths. Figs. 2 and 3 show the corresponding heat flux vs time curves (whose area gives total absorbed heat). Control functions for generating the optimal trajectories are given in Fig. 6 and 7 along with those for the nominal flight path. Figs. 8-12 show V, dV/dt, h, γ, and Q as functions of time for the OPT-I and nominal flight paths. Figs. 13-16 show the effects of the flares and dives on the heat flux, velocity, and density changes.

Comparison of Absorbed Heat Values and Cross Range Attained. The total absorbed heat, cross range, and their ratio are presented in Table 2 for the OPT-I, OPT-II, Sub-OPT-III, and Sub-OPT-IV flight paths as well as for the nominal trajectory. Compared to the nominal flight path, the optimal trajectories show both a substantial reduction in absorbed heat and an increase in cross range, reducing the total absorbed heat per cross range by 20 - 22%. The sub-optimal solutions (with non-optimal γ-entry, show far less improvement in the same terms. The reasons for these savings are discussed in the following sub-sections.

	Absorbed Heat <MJ/m^2>	Cross Range <km>
Nominal	723.8	2886
OPT-I	605.1 (-16.4%)	3103 (+7.5%)
OPT-II	594.0 (-17.8%)	2991 (+3.7%)
Sub-OPT-III	685.6 (-5.2%)	2970 (+2.9%)
Sub-OPT-IV	703.1 (-2.8%)	3050 (+5.7%)

	Absorbed Heat / Cross Range <MJ/m^2/ km>	
Nominal	0.2508	
OPT-I	0.1950	(-22.2%)
OPT-II	0.1988	(-20.7%)
Sub-OPT-III	0.2308	(-8.0%)
Sub-OPT-IV	0.2305	(-9.0%)

Table 2. Absorbed heat, cross range, and absorbed heat per cross range for the OPT-I, OPT-II, Sub-OPT-III, Sub-OPT-IV, and nominal trajectories.

Effects of Imposing a Thermal-α Corridor. The OPT-I and OPT-II trajectories are quite similar in structure. The difference in the two solutions arises due to the "release point" for the α control. OPT-II flies within a thermal-α corridor, restricting α to be > 25° as long as $\dot{Q} > 175$ KW/m^2. OPT-II actually has less total absorbed heat than OPT-I (594 vs 605 MJ/m^2), since the OPT-II trajectory flies higher than the OPT-I path as the heat flux nears the release point. (See Figs. 1 and 6.) However, the cross range for OPT-II suffers (2991 vs

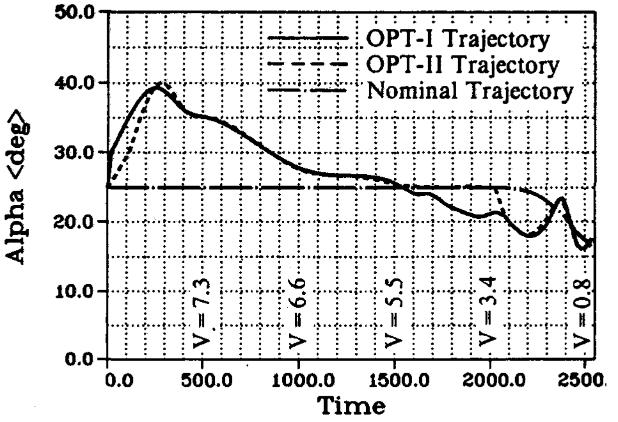

Fig. 6 Control function, α, as a function of time for the OPT-I, OPT-II, and nominal trajectories.

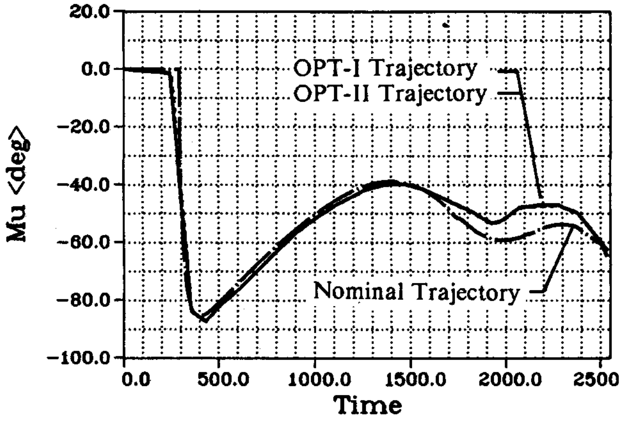

Fig. 7 Control function, μ, as a function of time for the OPT-I, OPT-II, and nominal trajectories.

3103 km). The effect of the imposition of the thermal-α corridor on the OPT-II trajectory is about a 2% increase in absorbed heat per cross range over that attained by the OPT-I flight path.

The Effect of γ-entry on the Total Absorbed Heat. In the OPT-I and OPT-II flight paths, γ-entry, selected by the optimization process, is -1.2°. The nominal flight path uses a value of -1.4°. Thus, flying the optimal trajectory, the spacecraft enters the atmosphere at a shallower angle and as a result flies through the very thin air (120 km to 90 km) higher than it would following the nominal trajectory, being 5 km higher as it starts the initial flare. The comparative density difference accounts for the slower build up of the heat flux. See Figs 1-2.

Thus, even in this flight regime of ineffective aerodynamic forces, heat flux control can be affected through the use of an optimal γ-entry, yielding a heat flux value of 150 KW/m^2 less than that of the nominal trajectory.

The Sub-OPT-III and -IV curves (Figs. 3-4), in contrast, first show a savings in absorbed heat when the aerodynamic forces become effective. There is no earlier heat flux control, and the resulting total absorbed heat

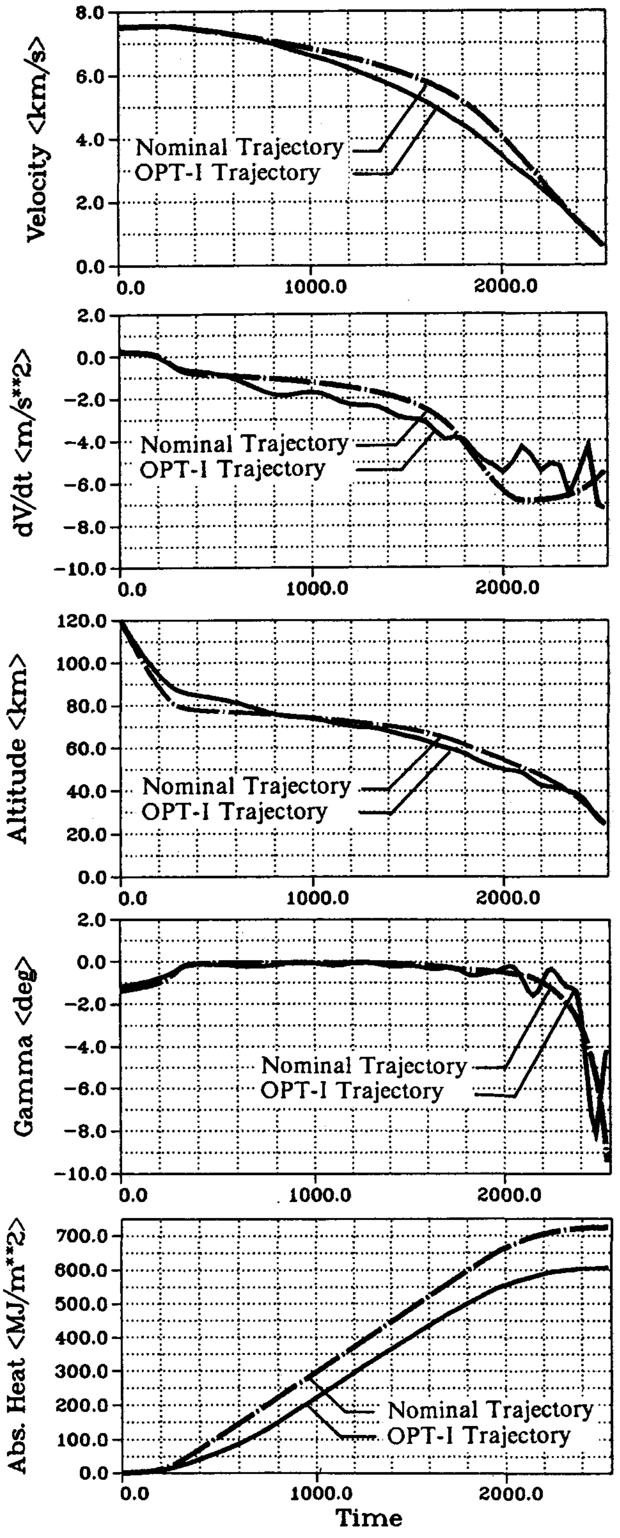

Figs. 8-12. Velocity, deceleration, altitude, gamma, and absorbed heat as functions of time for the OPT-I and nominal trajectories.

levels of the two sub-optimal solutions are significantly larger, 80-100 MJ/m^2 higher than those of the OPT-I, -II solutions. (These suboptimal solutions also yield less cross range.)

Thus, the selection of γ-entry can be used effectively to control heat build up in the very early stages of atmospheric flight.

The Effectiveness of the Initial Flare in Reducing the Total Absorbed Heat. The OPT-I, -II flight paths make their initial flare at a higher altitude than does the nominal trajectory, which approaches the thermal constraint (at ~78 km) and then flares. The OPT-I and -II paths begin to flare as soon the effects of the aerodynamic forces can be (even marginally) felt. (See Figs. 1-2.) The heat flux value has already been held below that of the nominal trajectory due to the shallower entry angle. The initial flare enhances this condition further.

The initial flare occurs between 250-425 sec into the atmospheric flight, as the altitude decreases from 90 to 83 km. The $\dot{Q}$ value rises during this time span but at a much slower rate than that of the nominal flight path. The effect of the flare is to change the curvature of heat flux, i.e., $\dot{Q}$ becomes "concave down" and as a result increases more slowly. Thus, even in this region of small aerodynamic forces, the flare produces a substantial savings in absorbed heat.

The Sub-Opt-III and -IV trajectories first show significant heat saving at the initial flare (80km). While the Sub-OPT-IV trajectory is a no-skip flight path, Sub-Opt-III has been allowed to skip slightly (less than 1°). This slight skip accounts for the large heat savings pocket in the "upper left hand corner" of the curves in Fig. 4. The flare is actually strong enough to cause a reduction in heat flux (although the net effect of the higher flare of OPT-I and -II plus optimal γ-entry is still more favorable. (Compare Figs. 1-4.)) The heat flux values of the no-skip Sub-OPT-IV flight path lie roughly half way between the nominal and Sub-OPT-III values, and the trajectory gains its advantages by extending cross range.

The Flare-Dive Sequence as a Braking/Cooling Technique. Both the optimal and sub-optimal trajectories employ a flare dive strategy throughout the flight paths. At higher altitudes, this appears as slight oscillations with much more distinct flares and dives developing as the atmospheric forces become more and more effective. This strategy has arisen from the optimization code itself and differs decidedly from the approach used during the nominal flight path. The effects of this flare-dive strategy need to be investigated further.

Fig. 13 presents $\dot{Q}$ as a function of time, with the flare segments shown as solid lines and dive segments as dotted lines. (The condition $d\gamma/dt=0$ defines the switching points between flares and dives, i.e., $d\gamma/dt>0$ (γ increasing) is a flare, while $d\gamma/dt<0$ (γ decreasing) is a dive.)

The flares serve as cooling phases. The curvature of $\dot{Q}$ in each flare is clearly concave down, which retards the rate of heat flux increase that had built up in the preceding dive segment. In the portion of the trajectory with high heat flux levels (t < 1700 sec), the flare "caps" the heat flux curve, i.e., the flare results in local heat flux maxima and affects a decrease which continues into the start of the dive (before the density changes in the dive enact a further heat flux build up). When aerodynamic effects have slowed the vehicle down enough that heat flux values can actually decrease continually, the flare segments form inflection points in $\dot{Q}$. More specifically, in the latter portion of the heat flux curve, the dive segements still have the undesirable curvature (concave up), but as the local minima resulting from the dives are reached, the subsequent flare affects a reversal in curvature, and the heat flux continues to decrease with little or no increase in $\dot{Q}$.

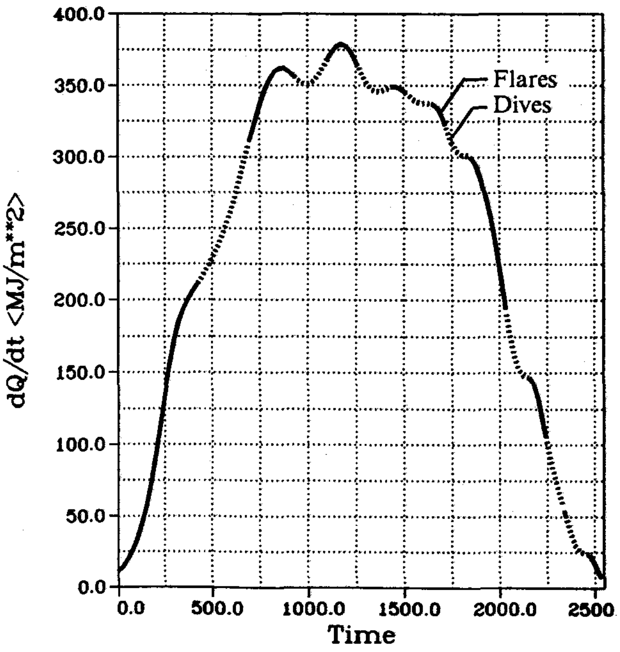

Fig. 13. Heat flux vs time for the OPT-I trajectory, showing the flare (solid lines) and dive (dotted lines) segments.

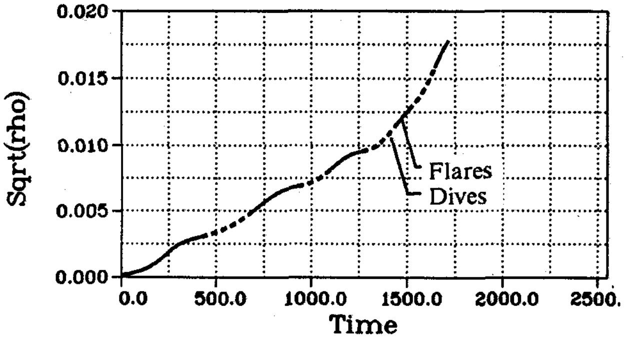

Fig. 14. $\sqrt{\rho}$ showing flare (solid lines) and dive (dotted lines) segments. (Inflections in $\sqrt{\rho}$ correspond to inflections in $\dot{Q}$.

$\dot{Q}$ is a function of both V^3 and $\sqrt{\rho}$. Fig. 15 shows that V^3 is essentially linear in the region of highest heat flux values, having a smooth curvature both initially and finally. On the other hand, $\le\overline{\rho}$ increases in an almost step like fashion (i.e., relatively level at the end of flare/transition to dive, but increasing in the dive itself). The curvature of $\dot{Q}$ is a function of both V and $\le\overline{\rho}$ along with the first and second derivatives of the terms. However, the dominant term in the curvature expression is $V^3 * d^2 \le\overline{\rho}\, /dt^2$. Thus, the curvature of $\dot{Q}$ depends upon the curvature of $\le\overline{\rho}$. When $\le\overline{\rho}$ is concave down (as in a flare), $\dot{Q}$ is also concave down, and when $\le\overline{\rho}$ is concave up (as in a dive), $\dot{Q}$ is also concave up. These curvature inflections are shown in Fig. 14 for the values $t < 1700$ s (marked for flares and dives) and in Fig. 16 for the entire flight.

The optimal flight paths experience good braking throughout the entire trajectory, and certainly the reduction of V^3 is essential for reducing the heat flux. However, it is the density term which accounts for the local maxima and minima in the heat flux curves. The concavity changes resulting from the flare and dive segments give the "pockets" of absorbed heat savings seen in Figs. 2 and 4.

Heat Flux Control: Comparing the Effects of the Optimal Flare-Dive Strategy to the Nominal Flight Path. Figs. 2 and 4 show that both the optimal and suboptimal solutions use a flare dive strategy whereas the nominal trajectory uses a smooth descent. These two approaches yield markedly different heat flux values. Figs. 15 and 16 compare optimal and nominal flight paths, showing the differences in the two contributing factors for heat flux, namely, V^3 and $\sqrt{\rho}$. During the initial flare and the ensuing dive, i.e., before significant deceleration has occurred, the OPT-1 flight path is at a higher altitude than the nominal path. Thus, density effects account for the differences in heat flux levels (and hence in absorbed heat). Although the differences in density are not large, the coupling with the extremely high velocity values (for both flight paths) accounts for sizable differences in absorbed heat build up.

From the start of the peak heat flux levels until nearly 2100 sec into the flight (i.e., until $\dot{Q}$ is below 150 KW/m^2), the velocity differences dominate the heat flux term. For the OPT-1 trajectory, the V^3 value decreases almost linearly in time, whereas the value for the nominal flight path decreases more slowly, lying well above that of the optimal trajectory. (The better braking effects of the optimal flight paths are also evident in Figs. 8 and 10.)

Thus, to control heat flux the optimal flight paths initially utilize density effects by flying at a higher altitude (a result of the initial flare). As the aerodynamic effects become stronger, the continued flare-dive sequences provide better deceleration than the smoother nominal flight path descent. This better deceleration controls the heat flux by reducing the V^3 value. In addition, the flare-dive combinations control the absorbed heat, by bringing about curvature changes in the heat flux profile through the $\sqrt{\rho}$ term (as described in the previous section).

VI. Conclusions

Optimal trajectories have been determined which minimize the total absorbed heat per cross range, i.e., which yield both low absorbed heat and large cross range. The flight paths have been analyzed from the deorbit point down to an altitude of 24.5 km, the onset of the terminal area energy management phase, ending with a Mach number of 2.0. No-skip trajectories have first been determined, and then slight skipping has been allowed to show the potential for reducing the heat flux using such a technique. The resulting flight paths have been compared with nominal trajectories developed previously using an engineering approach for selecting the control functions, α and μ. The optimal flight paths yield a reduction of more than 20% in the cost function. The results of the optimal flight paths are to be used as input for a possible redesign of the nominal flight path strategy.

Three important factors have been shown to be effective in reducing the total absorbed heat while still

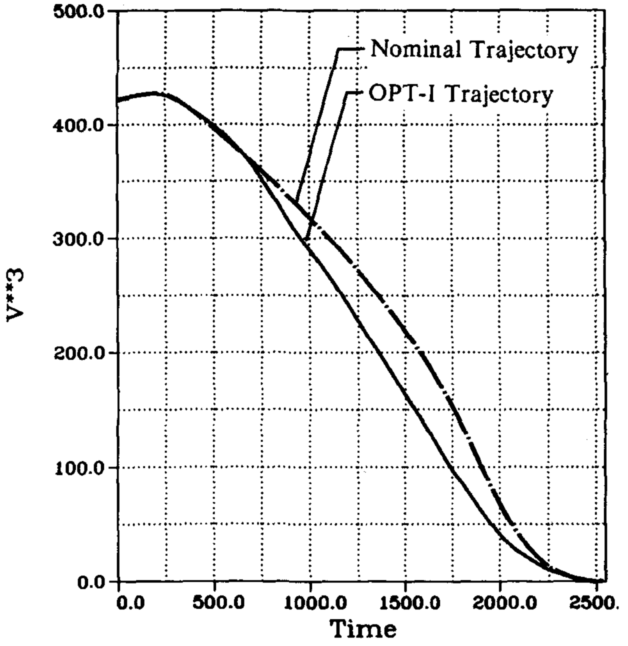

Fig. 15. Heat flux parameter, V^3 as a function of time for the OPT-1 and nominal trajectories.

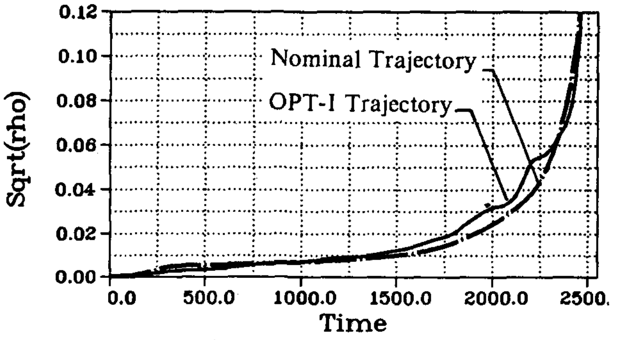

Fig. 16. Heat flux parameter, $\sqrt{\rho}$ as a function of time for the OPT-1 and nominal trajectories.

maintaining large cross range: (1) the value of γ-entry, (2) the altitude of the initial flare, and (3) the development of a flare-dive strategy. The first two factors make use of density effects to reduce heat flux, i.e., the spacecraft flies higher following such trajectories. As aerodynamic forces become effective, the optimal trajectories follow a flare-dive strategy, which provides better deceleration than does a smooth descent. The flare-dive flight path combines this improved braking with density changes to decrease the absorbed heat. The flares cause a reduction in heat flux rate through less altitude change. The dives increase the heat flux rate due to larger altitude changes. The combination of the flares and dives yields a heat flux profile with curvature reversal points which hold the heat flux values well below those of the nominal flight path, resulting in a substantial reduction in absorbed heat.

References

1. Kiefer, A., "Hermes 94 Nominal Trajectories (Status Report)," MBB-TN-Hermes-13, 17.01.89 .

2. Strohmaier, P., A. Kiefer, D. Burkhardt, and K. Horn, "Proceedings: AGARD-FMP Symposium, Space Vehicle Flight Mechanics," Luxembourg, 13-16 November, 1989.

3. Kraft, D., "FORTRAN Computer Programs for Solving Optimal Control Problems," DFVLR Report 80-03, 8031 Wessling/Obb., FRG, 1980.

4. Shampine, L. F. and H. A. Watts, "Practical Solutions of Ordinary Differential Equations by Runge-Kutta Methods," SAND 76-0585 (1976) Sandia National Laboratories, Albuquerque, New Mexico, USA, Dec. 1976.

5. Horn, M.K., "RKF45T - A Runge-Kutta 4/5 Software Package with User-Supplied Stops Involving the Dependent Variables and First Derivatives," DFVLR Internal Note, 515-83/3, 8013 Wessling/ Obb., FRG, 1983.